Electronic Supplementary Material (ESI) for Nanoscale.

Supporting Information

Bimetallic MOF-derived Hollow ZnNiC Nano-boxes for Efficient Microwave Absorption

P. Miao, J.-W. Cao, Prof. J. Kong, J. Li, Dr. T. Wang and Prof. K.-J. Chen**

Experimental Section

Material synthesis

All reagents were commercially purchased and used without further purification. Zinc acetate dihydrate ($Zn(CH_3COO)_2 \cdot 2H_2O$, 99.99%, metal basis) and nickel (II) acetylacetonate ($Ni(C_5H_7O_2)_2 \cdot 4H_2O$, 95%) were brought from Aladdin Corp., terephthalic acid (H_2BDC, 99%) was purchased from Macklin Corp., dimethylacetamide (DMAC, AR ≥ 98.5%) and ethyl alcohol absolute (C_2H_5OH, AR ≥ 99.7%) were obtained from GHTECH Corp.

Synthesis of hierarchical hollow ZnNi-MOF. The hollow ZnNi-MOF was synthesized via a simple hydrothermal reaction using an improved synthetic method.[1] Typically, Zn $(CH_3COO)_2$ (26 mg), $Ni(C_5H_7O_2)_2$ (52 mg), H_2BDC (17 mg), and DMAC/ethanol mixture (25 mL, v/v = 16:9) were dissolved in 50ml Teflon-lined autoclave and stirred for 20 min at room temperature (RT). The resultant mixture was sealed and then heated to 150 ºC for 3 h before it was cooled to RT. The dark green precipitation was obtained by centrifugation at 10000 rpm for 10 minutes and further purified with DMAC for three times.

ZnNi-MOF derived hollow ZnNiC nanocomplexes. The as-synthesized hollow ZnNi-MOF was loaded in the ceramic boat and put into a tube furnace (OTF-1200X, Kejing New Mater. Ltd., Hefei, China). The ZnNiC nanocomplex was obtained through the stepwise heating process (heating rate: 1 ºC min^{-1}) and maintained at 600 - 800 ºC for 2 h under an argon atmosphere.

Materials Characterization: The power X-Ray diffraction (PXRD) data of the off-white samples were collected by a Rigaku-MiniFlex 600 diffractometer equipped with the use of monochromatized Cu Kα radiation ($K\alpha_1$, λ = 1.540593Å) flux at a scanning rate of 5 ^oC min^{-1}. The thermogravimetric analysis (TGA) and mass spectrometry (MS) analysis were performed on a simultaneous thermal device (STA, 449C Jupiter, Netzsch, Gerätebau GmbH, Selb, Germany) combined with a quadrupole mass spectrometer (QMS, 403C Aëolos, Netzsch,

Germany) under a heating rate of 10 ºC min^{-1} at a range from 40 to 1200 ºC (Argon, 40 mL min^{-1}). Micromeritics 3Flex was used for collecting all adsorption and desorption isotherms for 77 K of N_2. The morphology and structure were examined using scanning electron microscopy (FESEM, Verios G4, FEI) and transmission electron microscopy (TEM, Talos F200X, FEI), and element mapping was scanned by TEM. The chemical valence of relative elements was detected through X-ray photoelectron spectroscopy (XPS) measurement on an Axis Ultra DLD spectrometer using monochromatic Al Kα radiation (hυ =1486.6 eV, Kratos, England). The carbon species were analyzed by Raman spectra (514 nm, Renishaw-invia, England) with an argon-ion laser. The magnetic property was carried out by a vibrating sample magnetometer (Quantum Design, America).

Microwave performance measurement. A vector network analyzer (VNA, MS4644A, Anritsu) was used to collect the electromagnetic parameters in the frequency range of 2 - 18 GHz. The hollow ZnNiC nanocomplex was dispersed in a paraffin matrix with a 50 % mass fraction, which was then compressed into coaxial rings with an inner diameter of 3.04 mm and an outer diameter of 7.0 mm.

$$Z_{in} = \sqrt{\frac{\mu_r}{\varepsilon_r}} \tanh\left[j \frac{2\pi fd}{c} \sqrt{\mu_r \varepsilon_r} \right] \qquad (1)$$

$$RL = 20 \log_{10} \left| \frac{Z_{in} - 1}{Z_{in} + 1} \right| \qquad (2)$$

$$\left(\varepsilon' - \frac{\varepsilon_s + \varepsilon_\infty}{2} \right) + (\varepsilon')^2 = \left(\frac{\varepsilon_s - \varepsilon_\infty}{2} \right)^2 \quad (3)$$

$$\alpha = \frac{\sqrt{2}\pi f}{c} \times \sqrt{(\mu''\varepsilon'' - \mu'\varepsilon') + \sqrt{(\mu''\varepsilon'' - \mu'\varepsilon')^2 + (\mu''\varepsilon' - \mu'\varepsilon'')^2}} \quad (4)$$

Where Z_{in}, $\mu_{r,}$ and ε_r are the normalized input impedance, permittivity, and permeability of the paraffined-based composite, respectively. The *f*, *d*, and c represent the microwave frequency, thickness (*m*) of sample and the velocity of the microwave in a vacuum, respectively. The ε_s and ε_∞ are the static permittivity and relative permittivity.

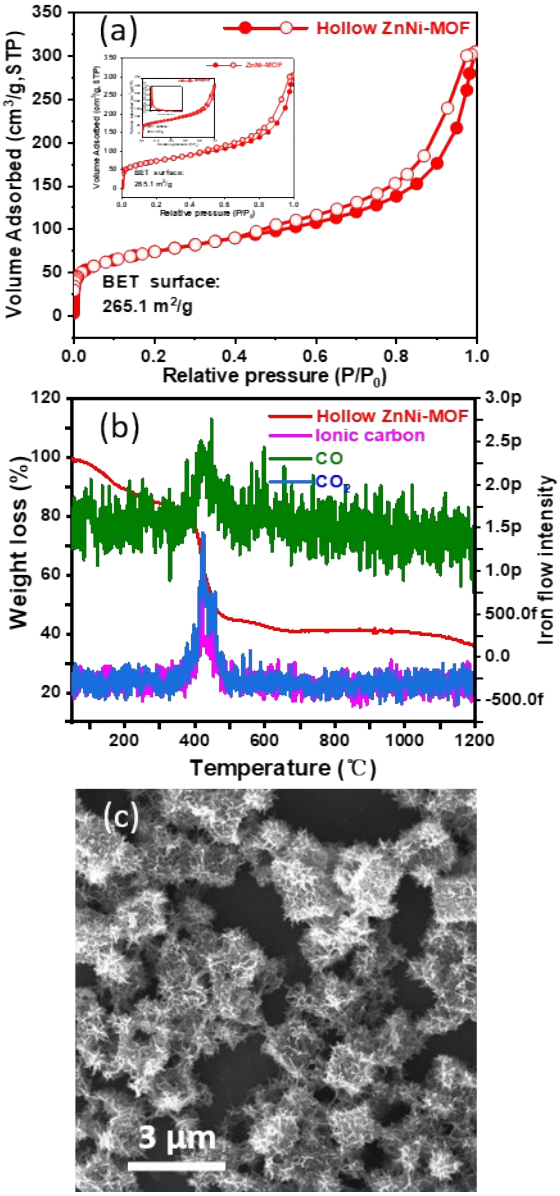

Figure S 1 (a) 77 K N_2 sorption, pore size distribution (inset), (b) TG-MS, and (c) SEM image of hollow ZnNi-MOF crystal.

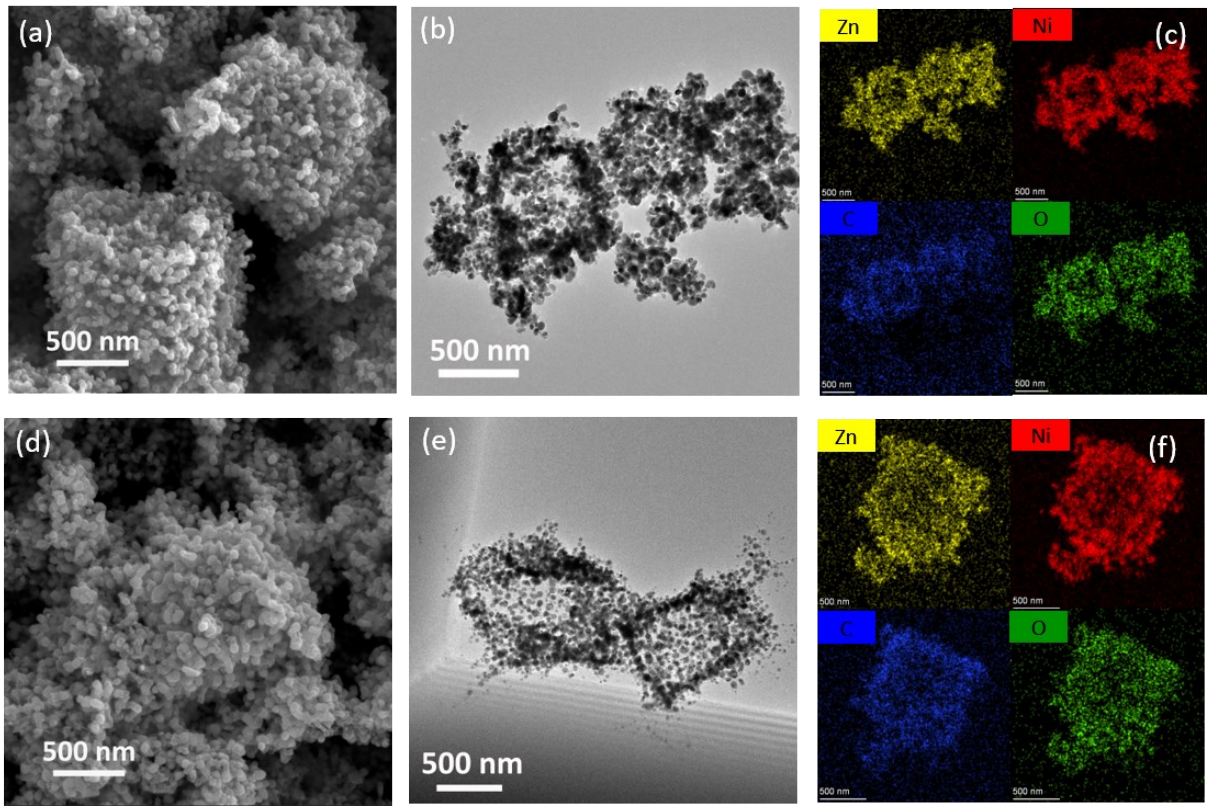

Figure S 2 (a) (d) high magnification of SEM images, (b) (e) TEM images, and (c) (f) element mapping (Zn, Ni, C, and O) of ZnNiC-700 and ZnNiC-800, respectively.

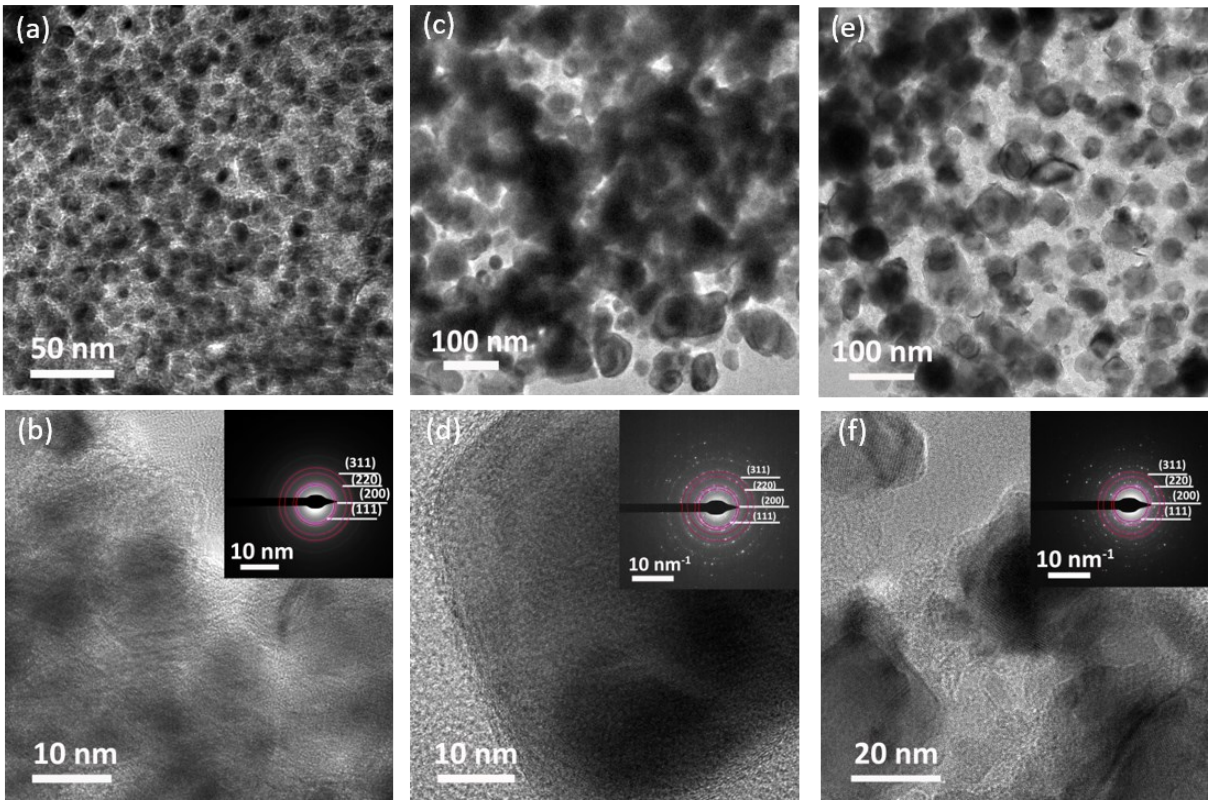

Figure S 3 The particles distribution, high-resolution images, and SAED images (inset) of ZnNiC-600 (a) (b), ZnNiC-700 (c) (d), and ZnNiC-800 (e) (f), respectively.

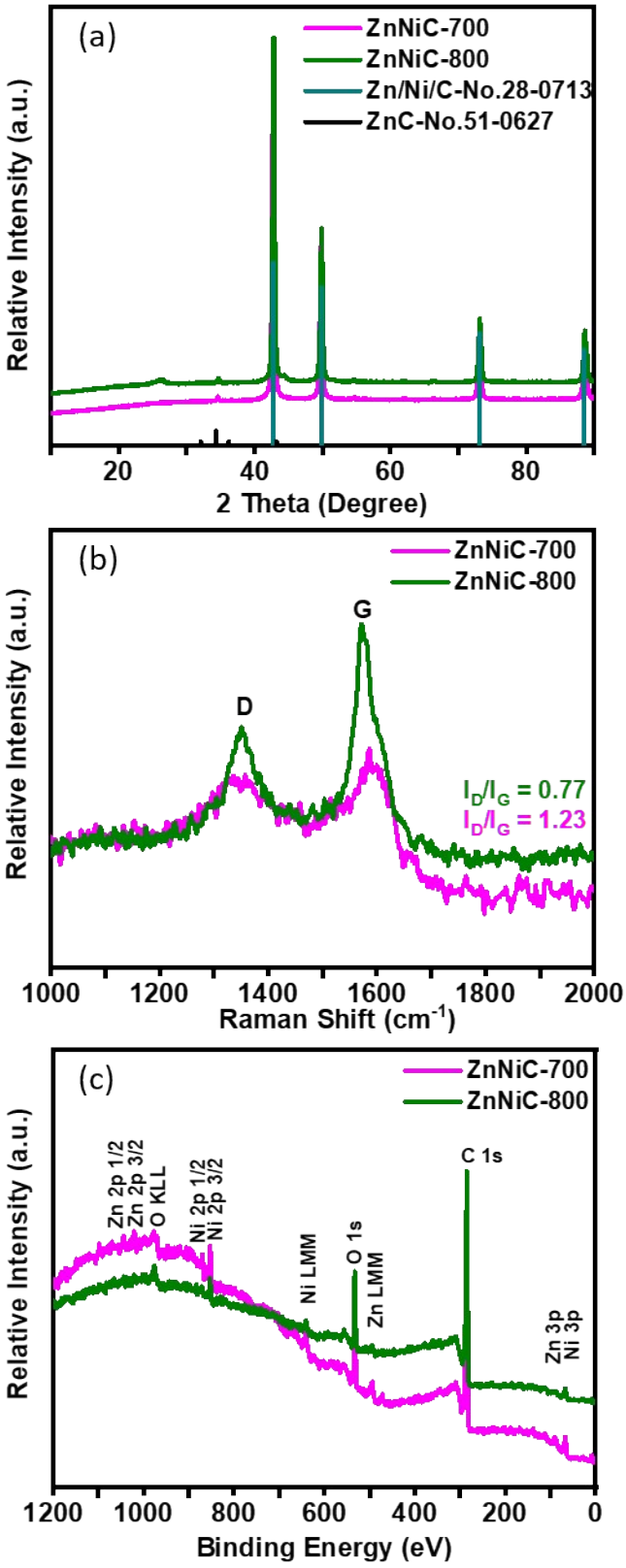

Figure S 4 The PXRD (a), Raman spectrum (b), and XPS spectrum (f) of ZnNiC-700, and ZnNiC-800, respectively.

When the pyrolysis temperature increases to 700 ºC, the evaporation of zinc atoms results in a higher value of I_D/I_G, which promotes more defective or disordered carbon in metal/carbon system synchronously. When pyrolysis temperature increased to 800 ºC, most of the defective and/or disorder carbon has transformed into graphite carbon rapdily, leading to decreased value of I_D/I_G.

Table S1 The semi-quantitative analysis of EDS for ZnNiC-600, ZnNiC-700, and ZnNiC-800, respectively.

Name[a]	C/%	O/%	Ni/%	Zn/%
ZnNiC-600	51.8	9.4	26.4	12.5
ZnNiC-700	43.8	2.9	39.9	13.34
ZnNiC-800	65.8	1.6	27.5	5.1

[a]atomic ratio

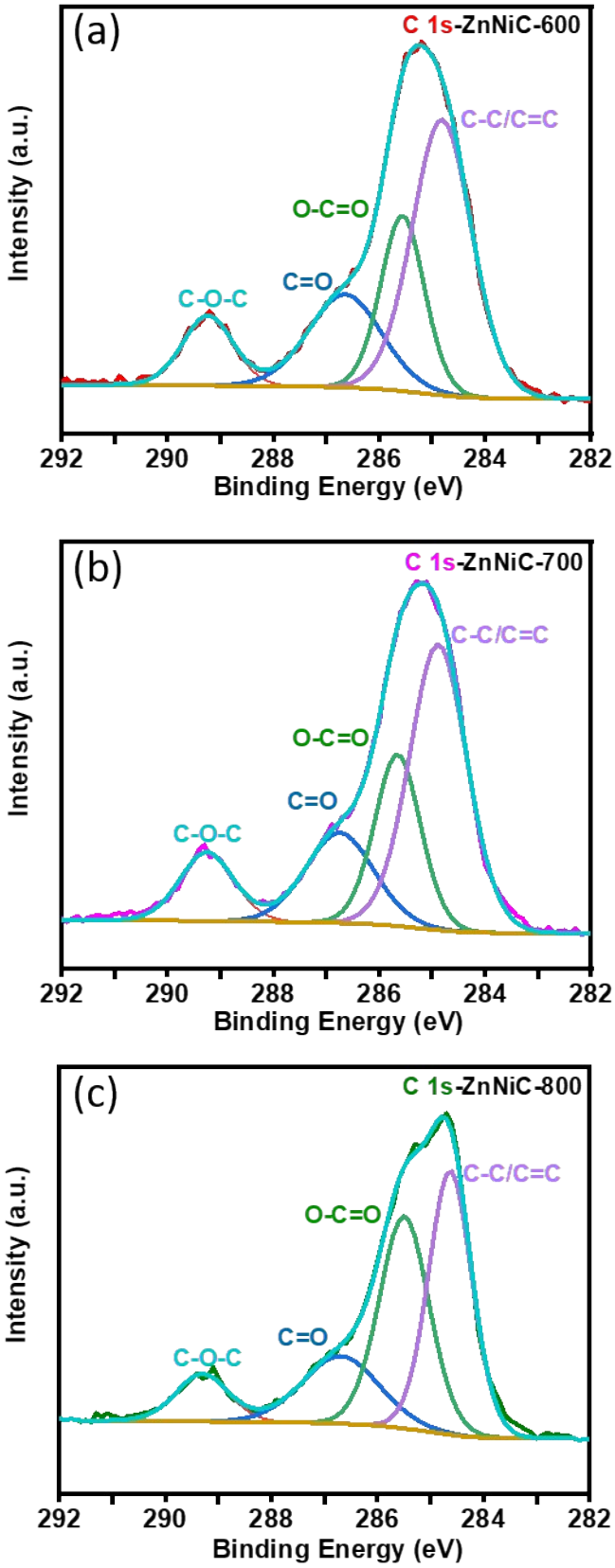

Figure S 5 The deconvolution of the C 1s spectrums of (a) ZnNiC-600, (b) ZnNiC-700, and (c) ZnNiC-800 nanocomplexes, respectively.

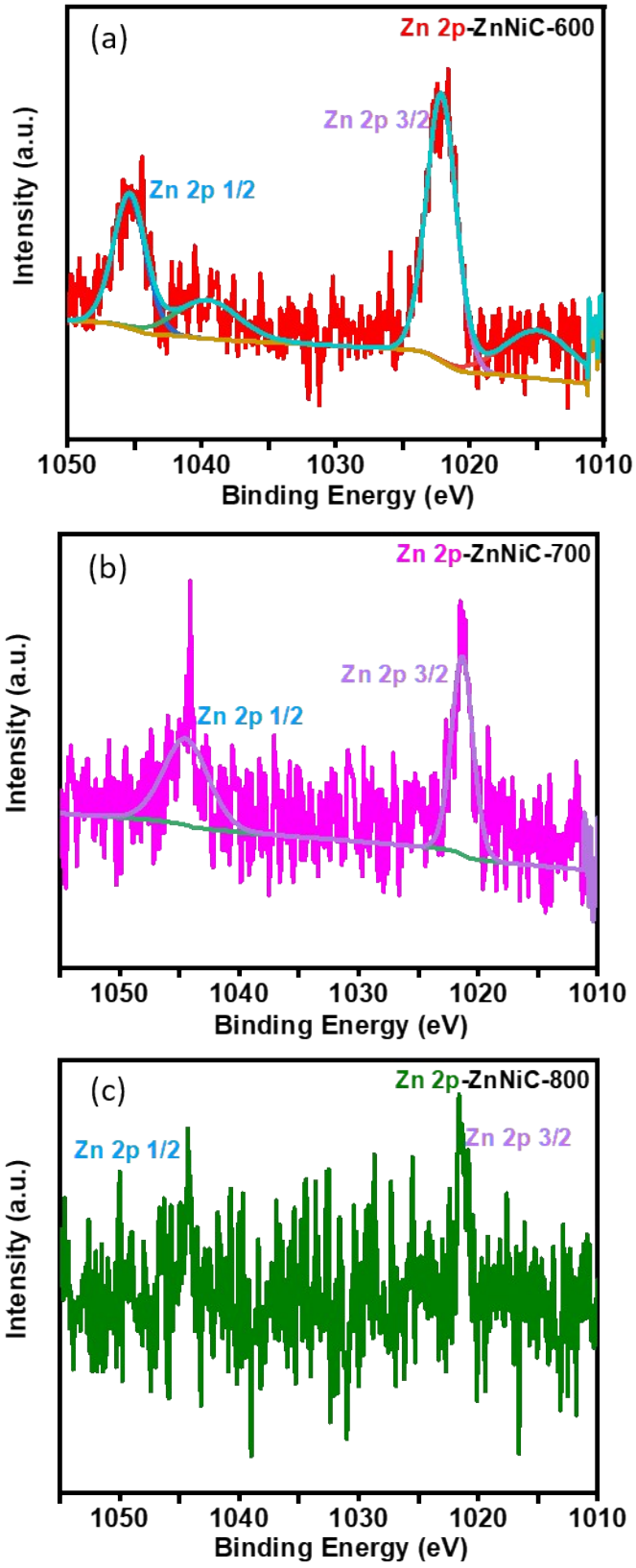

Figure S 6 The deconvolution of Zn 2p spectrums for ZnNiC-600, ZnNiC-700, and ZnNiC-800 nanocomplexes, respectively.

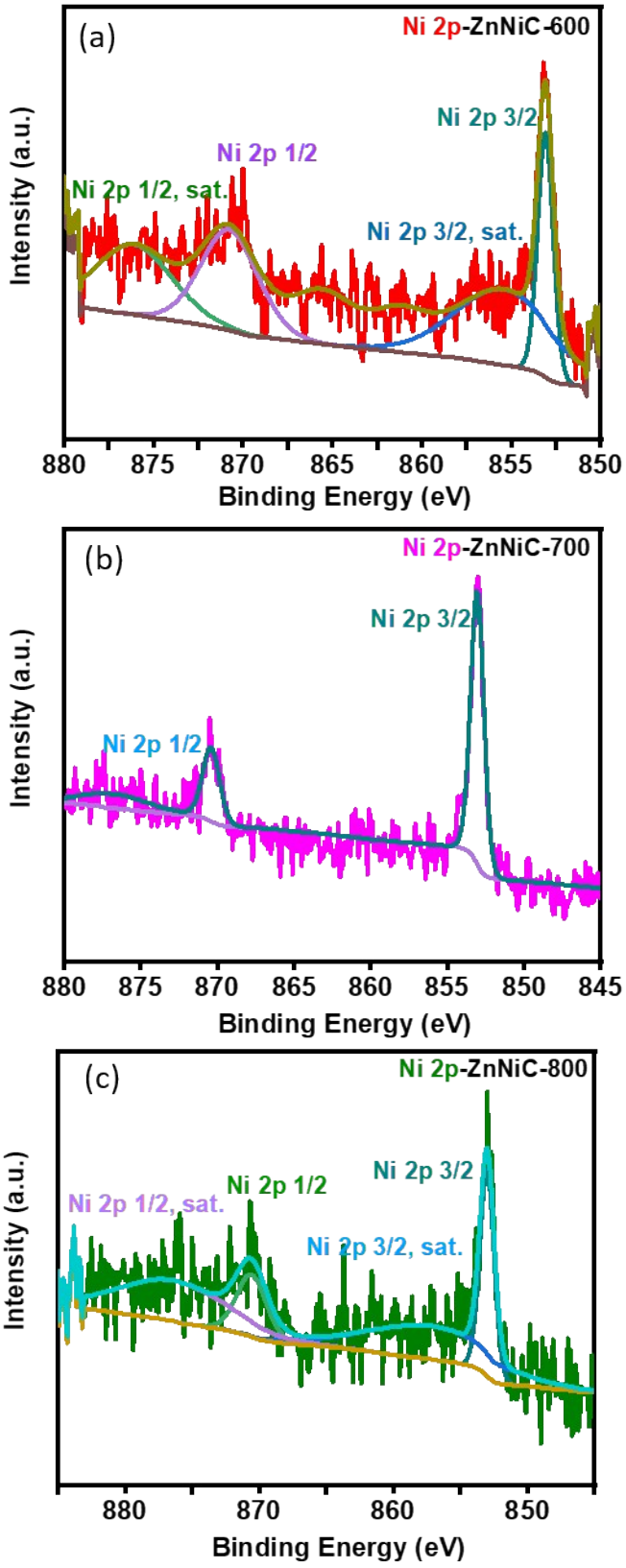

Figure S 7 The Ni 2p fitting spectrums of ZnNiC-600, ZnNiC-700, and ZnNiC-800, respectively.

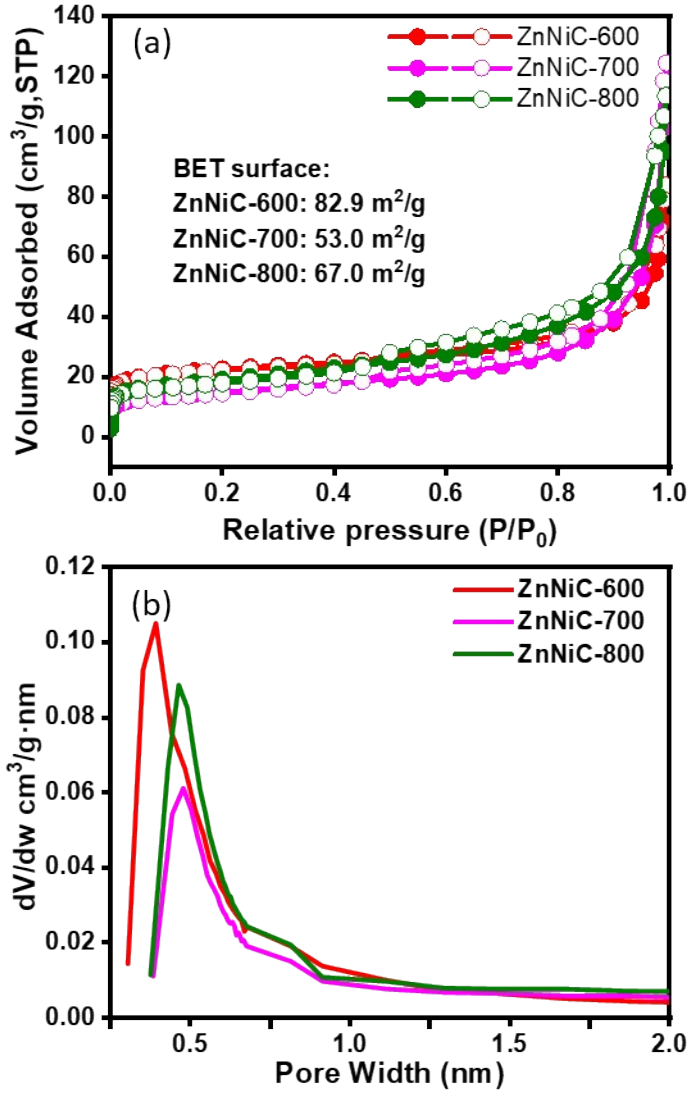

Figure S 8 The 77 K N_2 soprtion (a) and pore size distribution (b) of ZnNiC-600, ZnNiC-700, and ZnNiC-800, respectively.

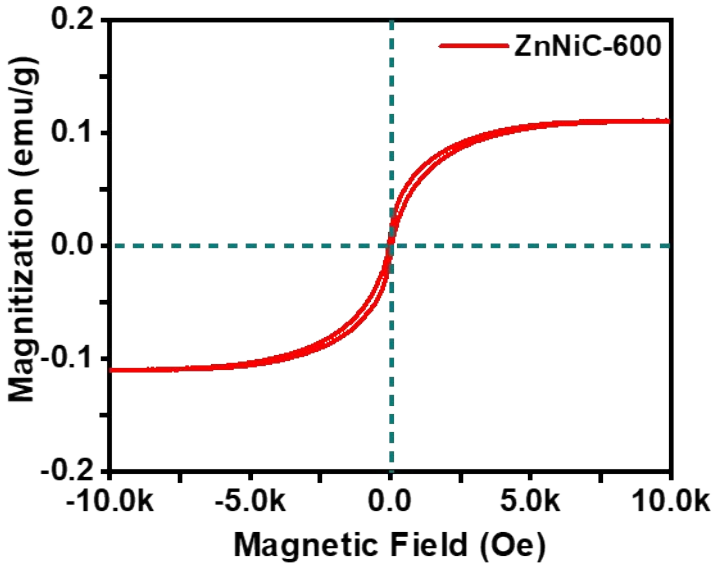

Figure S 9 The hysteresis loop of hollow ZnNiC-600.

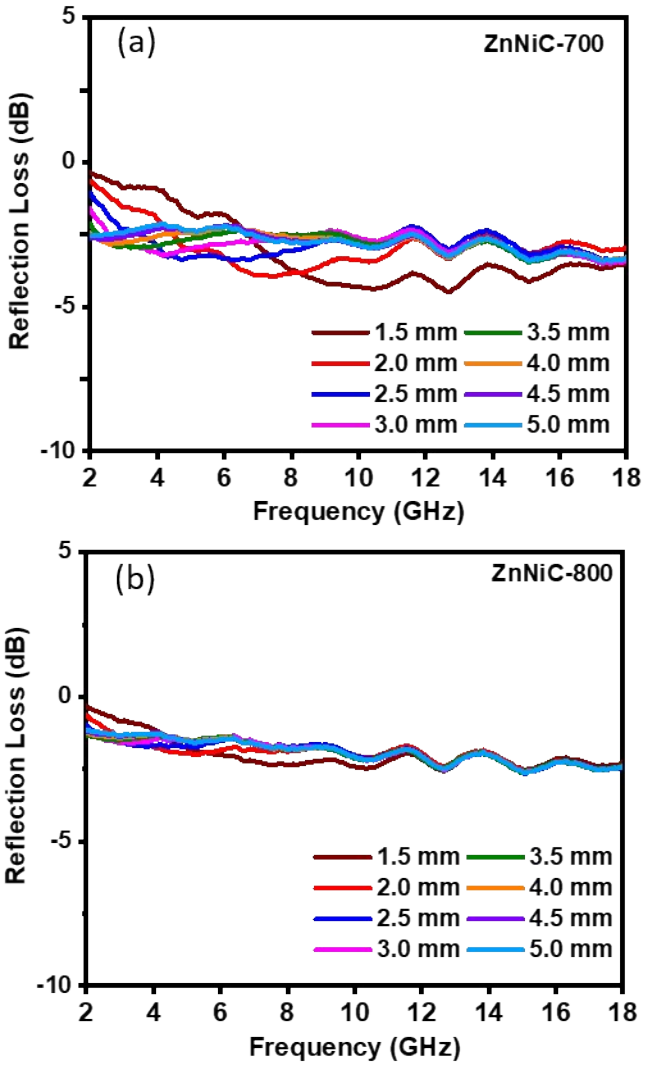

Figure S 10 The reflection loss (RL) of (a) ZnNiC-700, and (b) ZnNiC-800, respectively.

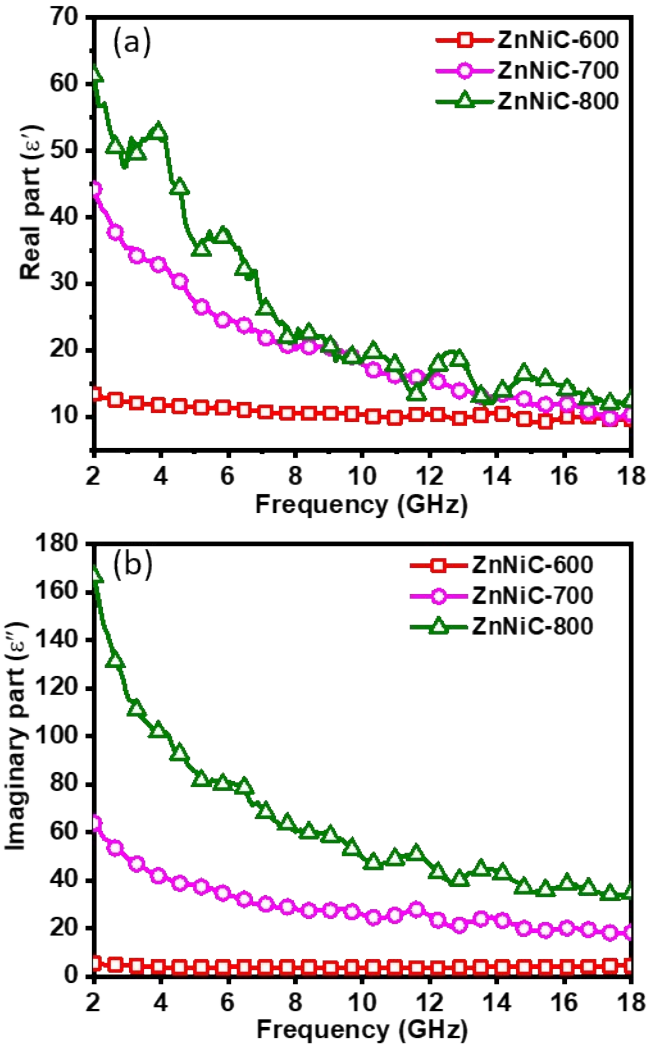

Figure S 11 The (a) real part and (b) imaginary part of complex permittivity for ZnNiC-600, ZnNiC-700, and ZnNiC-800, respectively.

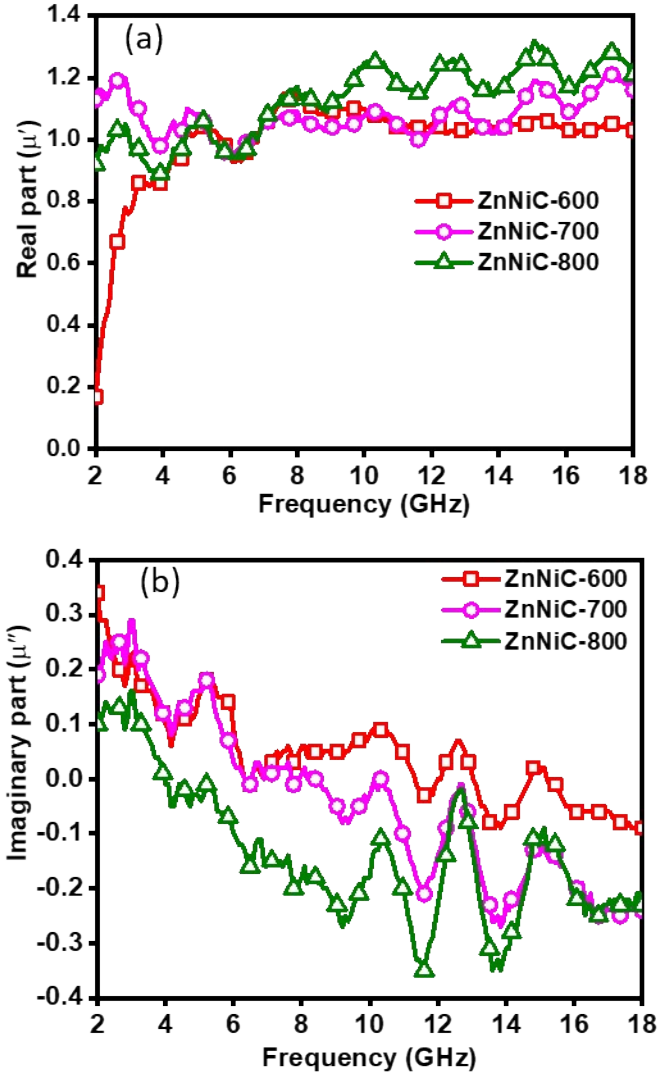

Figure S 12 (a) real part and (b) imaginary part of complex permeability for ZnNiC-600, ZnNiC-700, and ZnNiC-800, respectively.

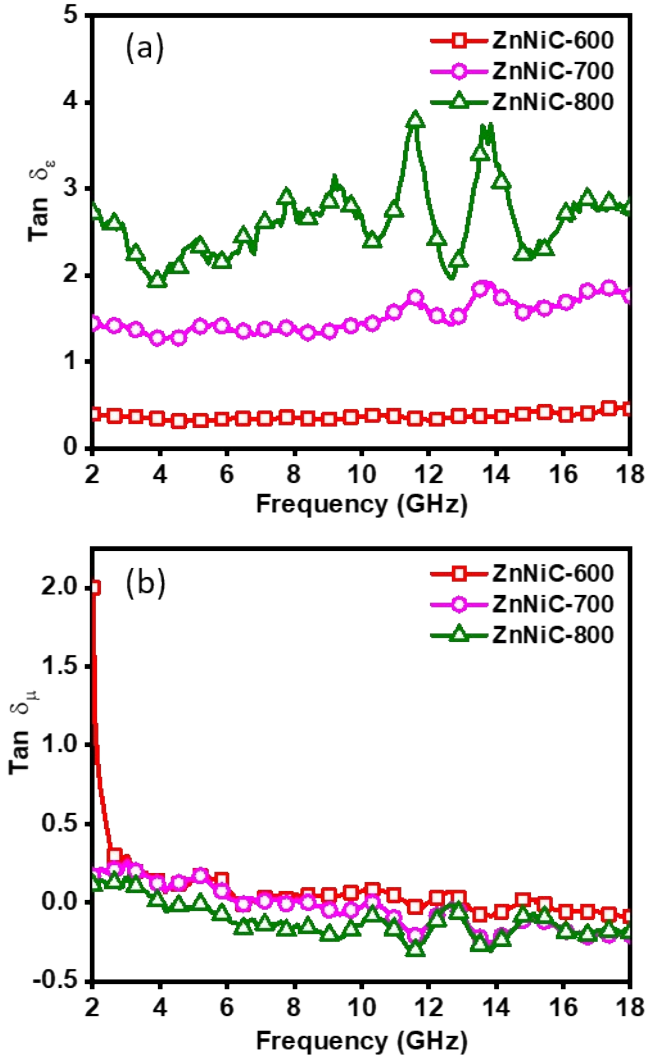

Figure S 13 (a) tangent δ_ε value, and (b) tangent δ_μ value of for ZnNiC-600, ZnNiC-700, and ZnNiC-800, respectively.

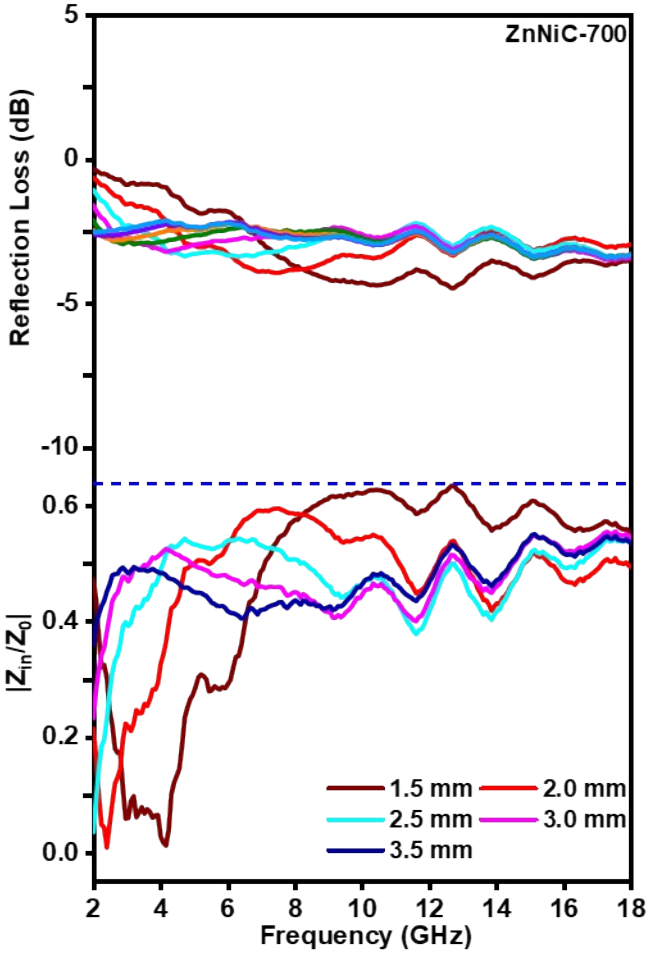

Figure S 14 The reflection loss and normalized input impedance of ZnNiC-700 nanocomplexes.

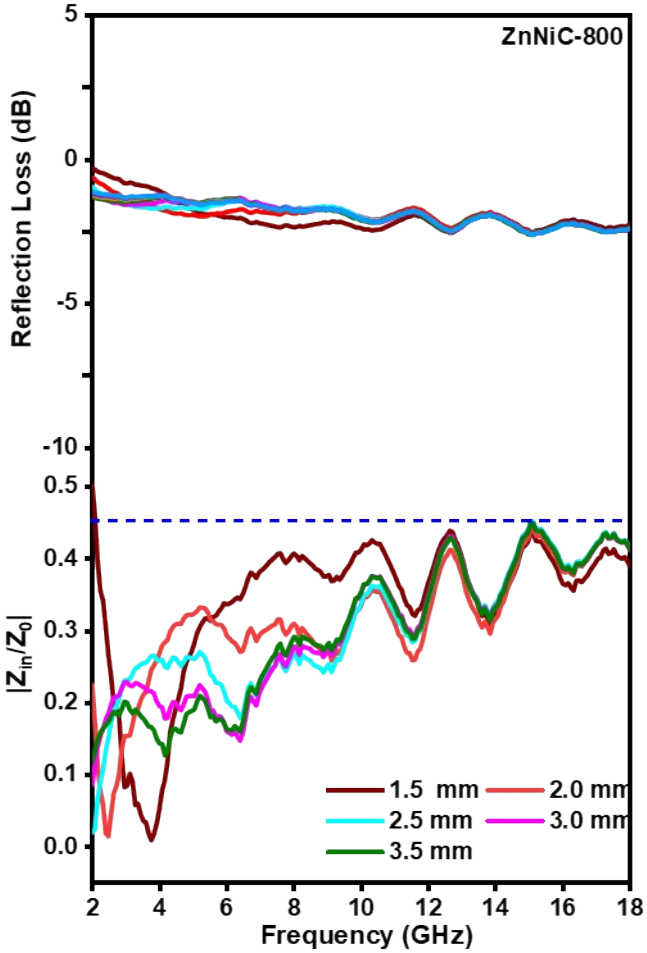

Figure S 15 The reflection loss and normalized input impedance of ZnNiC-800 nanocomplexes.

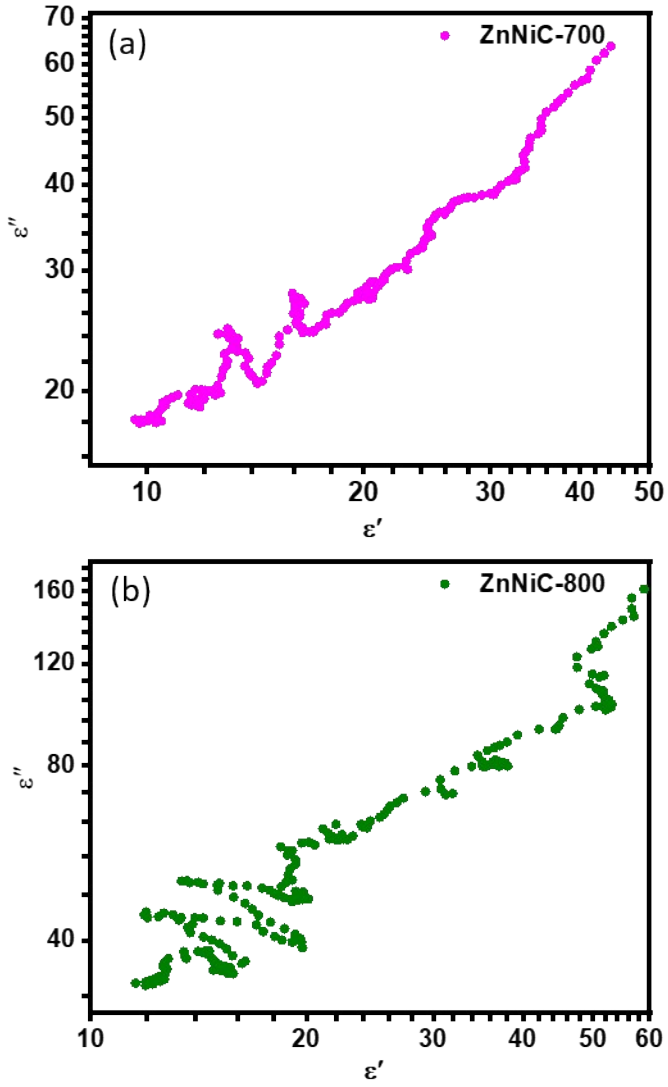

Figure S 16 The Cole-Cole plots of ZnNiC nanocomplexes: (a) ZnNiC-700, and (b) ZnNiC-800 in the frequency range of 2-18 GHz.

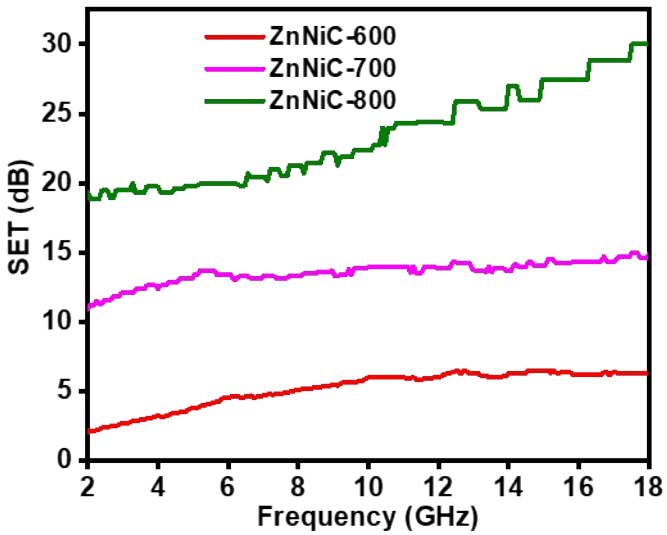

Figure S 17 The electromagnetic shielding efficiency of ZnNiC-600, ZnNiC-700, and ZnNiC-800, respectively.

ZnNiC-700 and ZnNiC-800 shield more than 90% of microwave. With the increase of pyrolysis temperature, the graphitization degree increases gradually, resulting in high complex permittivity (Figure S11). The values of $|Z_{in}/Z_o|$ of ZnNiC-700 and ZnNiC-800 were 0.4-0.6 and 0.2-0.4 (Figure S15), respectively. With the lower values of $|Z_{in}/Z_o|$, the impedance mismatch in ZnNiC-700 and ZnNiC-800 will cause more reflections occurrence, rather than introduce microwave into particle, when the microwave reaches the particle surface. As a result, the electromagnetic shielding effect takes the dominate role for ZnNiC-700 and ZnNiC-800.

Table S2 The summary of pure MOFs as precorsors deriving nanocomposite for microwave absorption

Precursor	RL/dB	Thickness/mm	EAB(GHz)	Loading/%	Ref.
Prussian blue	-22.6	2.0	7.2	40	2
HKUST-1	-12	1.85	5.7	40	3
Ni-ZIF	-86.8	2.7	7.4	40	4
CoNi-BDC	-51	1.5	4.5	30	5
CoZr-UIO-66	-57.2	3.3	11.9	50	6
Ni-MOF-24	-55.7	1.85	6.0	30	7
CoZn-ZIF	-59.7	1.5	5.3	30	8
MIL-88A	-52.9	3.07	4.64	40	9
MIL-101	-65.5	3.0	4.5	40	10
MOF-71	-49.76	1.76	5.44	30	11
Ni-BTC	-57.25	1.8	5.1	30	12
Co-MOF-74	-62.12	2.4	4.6	30	13
NiZn-MOF	-55.8	2.5	4.1	25	14
ZIF-67	-35.3	2.5	5.8	40	15
CPT-1-Co	-15.7	1.7	5.4	30	16
ZIF-67s	-53.0	1.8	6.2	30	17
ZnNi-MOF	-66.1	1.6	4.3	50	This work

Table S3 MA performance of typical hollow absorbers.

Hollow Absorbers	RL/dB	Thickness/mm	EAB/GHz	Loading/%	Ref.
Ni/SnO_2	-36.7	1.7	3.4	50	18
$ZnxFe_{3-x}O_4$	-18	3.4	5.12	65	19
CuS	-17.5	1.1	2.6	50	20
flower-like CuS	-31.5	1.8	3.6	30	21
$CoFe_2O_4$	-18.5	2.0	3.7	60	22
Graphene-wrapped ZnO	-45.1	2.2	2.5	50	23
Cobalt spheres	-47.0	1.5	4.6	30	24
Ni/C microspheres	-57.3	1.8	5.1	30	12
FeCoNi@C	-64.8	2.1	8.08	38	25
$Co/C@V_2O_3$	-40.1	1.5	4.64	50	26

Reference

1 Z. Zhang, Y. Chen, S. He, J. Zhang, X. Xu, Y. Yang, F. Nosheen, F. Saleem, W. He and X. Wang, *Angew. Chem. Int. Ed.*, 2014, **53**, 12517-12521.

2 R. Qiang, Y. C. Du, H. T. Zhao, Y. Wang, C. H. Tian, Z. G. Li, X. J. Han and P. Xu, *J. Mater. Chem. A*, 2015, **3**, 13426-13434.

3 W. Liu, L. Liu, Z. Yang, J. Xu, Y. Hou and G. Ji, *ACS Appl. Mater. Interfaces*, 2018, **10**, 8965-8975.

4 J. Yan, Y. Huang, Y. H. Yan, L. Ding and P. B. Liu, *ACS Appl. Mater. Interfaces*, 2019, **11**, 40781-40792.

5 J. Xiong, Z. Xiang, J. Zhao, L. Z. Yu, E. B. Cui, B. W. Deng, Z. C. Liu, R. Liu and W. Lu, *Carbon*, 2019, **154**, 391-401.

6 X. Zhang, J. Qao, J. B. Zhao, D. M. Xu, F. L. Wang, C. Liu, Y. Y. Jiang, L. L. Wu, P. Cui, L. F. Lv, Q. Wang, W. Liu, Z. Wang and J. R. Liu, *ACS Appl. Mater. Interfaces*, 2019, **11**, 35959-35968.

7 Z. L. Zhang, Q. H. Zhu, X. Q. Chen, Z. Wu, Y. Y. He, Y. Y. Lv, L. Zhang and Y. H. Zou, *Appl. Phys. Express*, 2019, **12**, 011001-011006.

8 W. Feng, Y. Wang, J. Chen, B. Li, L. Guo, J. Ouyang, D. Jia and Y. Zhou, *J. Mater. Chem. C*, 2018, **6**, 10-18.

9 N. Wu, D. Xu, Z. Wang, F. Wang, J. Liu, W. Liu, Q. Shao, H. Liu, Q. Gao and Z. Guo, *Carbon*, 2019, **145**, 433-444.

10 Z. Xiang, Y. Song, J. Xiong, Z. Pan, X. Wang, L. Liu, R. Liu, H. Yang and W. Lu, *Carbon*, 2019, **142**, 20-31.

11 Y. Zhang, H.-B. Zhang, X. Wu, Z. Deng, E. Zhou and Z.-Z. Yu, *ACS Appl. Nano Mater.*, 2019, **2**, 2325-2335.

12 Y. Qiu, Y. Lin, H. B. Yang, L. Wang, M. Q. Wang and B. Wen, *Chem. Eng. J.*, 2020, **383**, 123207-123219.

13 K. Wang, Y. Chen, R. Tian, H. Li, Y. Zhou, H. Duan and H. Liu, *ACS Appl. Mater. Interfaces*, 2018, **10**, 11333-11342.

14 L. Wang, X. Yu, X. Li, J. Zhang, M. Wang and R. Che, *Chem. Eng. J.*, 2020, **383**, 123099-123109.

15 Y. Lu, Y. Wang, H. Li, Y. Lin, Z. Jiang, Z. Xie, Q. Kuang and L. Zheng, *ACS Appl. Mater. Interfaces*, 2015, **7**, 13604-13611.

16 B. Y. Zhu, P. Miao, J. Kong, X. L. Zhang, G. Y. Wang and K.-J. Chen, *Cryst. Growth Des.*, 2019, **19**, 1518-1524.

17 M. Huang, L. Wang, K. Pei, W. You, X. Yu, Z. Wu and R. Che, *Small*, 2020, **14**, 2000158-2000169.

18 B. Zhao, W. Zhao, G. Shao, B. Fan and R. Zhang, *Dalton Trans*, 2015, **44**, 15984-15993.

19 Z. Yang, Z. Li, Y. Yang and Z. J. Xu, *ACS Appl. Mater. Interfaces*, 2014, **6**, 21911-21915.

20 B. Zhao, X. Guo, Y. Zhou, T. Su, C. Ma and R. Zhang, *CrystEngComm*, 2017, **19**, 2178-2186.

21 B. Zhao, G. Shao, B. Fan, W. Zhao, Y. Xie and R. Zhang, *J. Mater. Chem. A*, 2015, **3**, 10345-10352.

22 M. Fu, Q. Jiao, Y. Zhao and H. Li, *J. Mater. Chem. A*, 2014, **2**, 735-744.

23 M. Han, X. Yin, L. Kong, M. Li, W. Duan, L. Zhang and L. Cheng, *J. Mater. Chem. A*, 2014, **2**, 16403-16409.

24 C. He, S. Qiu, X. Wang, J. Liu, L. Luan, W. Liu, M. Itoh and K. I. Machida, *J. Mater. Chem.*, 2012, **22**, 22160-22167.

25 J. Ouyang, Z. L. He, Y. Zhang, H. M. Yang and Q. H. Zhao, *ACS Appl. Mater. Interfaces*, 2019, **11**, 39304-39314.

26 C. H. Zhou, C. Wu, D. Liu and M. Yan, *Chem-Eur. J.*, 2019, **25**, 2234-2241.